Atomic antisite disorder induced spin rearrangement in $CaZnFe_2O_5$

Maocai Pi,[1,2] Junye Yang,[3,4] Feiran Shen,[4] Shuai Tang,[1,2] Xubin Ye,[1] Lunhua He,[1,4] Zhiwei Hu,[5] Chang-Yang Kuo,[6,7] Chien-Te Chen,[6] A. E. Lebedeva,[8] S. V. Streltsov,[8] Zhao Pan,[1,2,*] Yao Shen,[1,2,†] and Youwen Long[1,2,‡]

[1]*Beijing National Laboratory for Condensed Matter Physics, Institute of Physics, Chinese Academy of Sciences, Beijing 100190, China*
[2]*School of Physical Sciences, University of Chinese Academy of Sciences, Beijing 100049, China*
[3]*Institute of High Energy Physics, Chinese Academy of Sciences, Beijing 100049, China*
[4]*Spallation Neutron Source Science Center, Dongguan 523803, China*
[5]*Max Planck Institute for Chemical Physics of Solids, Dresden 01187, Germany*
[6]*National Synchrotron Radiation Research Center, Hsinchu 300, Taiwan*
[7]*Department of Electrophysics, National Yang Ming Chiao Tung University, Hsinchu 30010, Taiwan*
[8]*M. N. Mikheev Institute of Metal Physics UB RAS, Ekaterinburg 620137, Russia*

(Received 29 October 2025; revised 6 August 2026; accepted 11 August 2026; published 28 August 2026)

Antisite disorder is a crystallographic defect that normally disrupts lattice continuity and dilutes magnetism. However, in some rare cases, instead of being suppressed, the spin order is reconfigured by antisite disorder, the detailed process of which, as well as the microscopic mechanism for the presence of antisite disorder, remains elusive. Here, we address these issues by investigating a newly synthesized postspinel oxide $CaZnFe_2O_5$, prepared through a high-pressure and high-temperature approach. Combined neutron diffraction and bulk magnetization measurements reveal A-type magnetic order below $T_N \approx 190$ K, accompanied by a small uniform spin canting, possibly triggered by Dzyaloshinskii–Moriya interactions. Meanwhile, neutron refinement reveals a pronounced Zn^{2+} and Fe^{3+} antisite disorder by 1/3, which, corroborated by Heisenberg model simulations, reshapes the competing exchange interaction network, converting the otherwise incommensurate magnetic ground state into an A-type spin configuration. First-principles calculations yield a much smaller energy increase in $CaZnFe_2O_5$ (89 meV per formula unit, f.u.) than in $CaCuFe_2O_5$ (340 meV/f.u.) upon antisite defect, providing quantitative support for the role of the lack of a Jahn–Teller distortion in facilitating the pronounced Zn and Fe antisite disorder, which profoundly impacts the macroscopic magnetic properties by reconfiguring exchange pathways.

DOI: 10.1103/vtv1-5pdk

I. INTRODUCTION

Antisite disorder refers to the occupation of crystallographic sites by alternative atomic species, disrupting translational symmetry and introducing local chemical and structural inhomogeneity [1,2]. Although such defects are typically unfavorable for investigating intrinsic physical properties of material systems, sometimes they may unexpectedly enhance material performance [1,3,4]. For instance, in the thermoelectric material SnTe, Sn and Te antisite defects significantly improve the Seebeck coefficient and overall power factor, thereby enhancing the thermoelectric performance [5]. In another aspect, magnetic systems often experience magnetic dilution due to antisite disorder, which is destructive for long-range magnetic order [6,7]. However, under certain circumstances, antisite defects can trigger extra exchange interactions and consequently spin reconfigurations [6–11]. In $MnSb_2Te_4$, for example, Mn and Sb antisite disorder bridges two-dimensional (2D) magnetic motifs, which elevates the magnetic transition temperature and the saturation magnetization [12]. These cases show that antisite disorder strongly influences the magnetic ground state; however, the microscopic mechanisms and the factors controlling the occurrence of antisite disorder remain unclear.

In this regard, postspinel oxides with the general formula AMM'_2O_5 (A: alkaline-earth metal, M and M': divalent and trivalent cations, respectively) provide a desirable platform for investigating antisite disorder. In the ideal structure, the M^{2+} ions occupy the 4a Wyckoff positions and the M'^{3+} cations reside on the 8f sites [Figs. 1(a) and 1(b)] [13–15]. An interesting example is $CaFe_3O_5$ (i.e., $CaFe^{2+}Fe_2^{3+}O_5$), which undergoes a magnetic transition at $T_N \approx 302$ K and displays a strong sensitivity to stoichiometry and cation distribution. For stoichiometric $CaFe_3O_5$, a site-ordered phase has been reported, in which Fe^{2+} and Fe^{3+} ions orderly occupy the 4a and 8f sites and the magnetic propagation vector $\boldsymbol{k} = (1/2, 0, 0)$ is accompanied by a sizable lattice distortion [13]. Others report an antisite-disordered phase involving the 4a and 8f sites with $\boldsymbol{k} = (0, 0, 0)$ in nonstoichiometric or nominal $CaFe_3O_5$, coexisting with the site-ordered phase [16]. In another aspect, $CaCuFe_2O_5$ (i.e., $CaCu_{2+}Fe_2^{3+}O_5$) undergoes a long-range antiferromagnetic (AFM) transition at $T_N \approx 165$ K

*Contact author: zhaopan@iphy.ac.cn
†Contact author: yshen@iphy.ac.cn
‡Contact author: ywlong@iphy.ac.cn

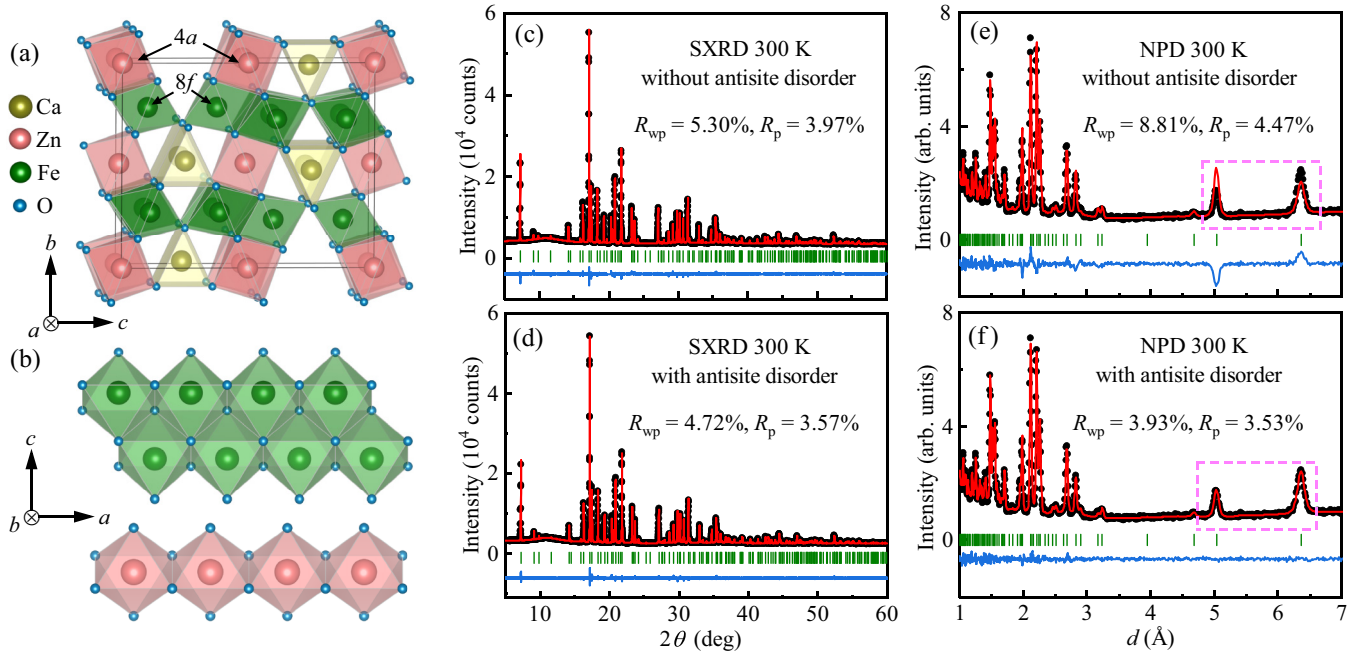

FIG. 1. (a) Schematic of the nominal orthorhombic $CaZnFe_2O_5$ structure without considering antisite disorder. (b) Sketch of the Fe_2O_5 zigzag spin ladder and ZnO_6 spin chain. The refinement results of (c), (d) SXRD and (e), (f) NPD for $CaZnFe_2O_5$ at 300 K without and with antisite disorder, respectively. The observed (black dot), calculated (red line), and difference (blue line) profiles are shown. The green ticks indicate the allowed Bragg reflections with space group *Cmcm*. The fitting quality for NPD can be significantly improved by considering Zn and Fe antisite occupation.

with a propagation vector $\boldsymbol{k} = (1, 0, 0)$ and shows no evidence of an antisite disordered phase at all [15]. The origin of these different behaviors, as well as the driving forces behind the presence or absence of antisite disorder, remains unresolved.

Here, by substituting the magnetic Fe^{2+} ions with nonmagnetic Zn^{2+}, we have successfully synthesized a new compound $CaZnFe_2O_5$. The introduction of nonmagnetic Zn^{2+} ions allows us to explore the interplay between lattice-site occupancy and magnetic exchange couplings. Our structural analysis reveals a pronounced Zn^{2+} and Fe^{3+} antisite disorder, along with a three-dimensional (3D) AFM order with $\boldsymbol{k} = (0,0,0)$ below $T_N \approx 190$ K, similar to that observed in nominal $CaFe_3O_5$. This is in sharp contrast to the incommensurate (IC) 2D magnetic order expected in the absence of antisite disorder. We attribute the pronounced antisite disorder in $CaZnFe_2O_5$ to the Jahn–Teller (JT) inactivity of the Zn^{2+} ion, which prevents it from preferably occupying the more distorted 4*a* site. Our findings thus establish a novel mechanism whereby JT inactivity promotes antisite disorder, and consequently reconfigures the magnetic exchange network.

II. METHODS

Polycrystalline $CaZnFe_2O_5$ samples were prepared with a high-pressure and high-temperature method. High-purity (>99.99%) starting materials, CaO, ZnO, and Fe_2O_3 powder, were mixed with a 1 : 1 : 1 mole ratio and thoroughly ground in an agate mortar within an argon-filled glovebox. Then the mixture was sealed into a platinum capsule with a diameter and height of 3.0 mm and treated at 7 GPa and 1423 K for 30 minutes in a cubic anvil-type high-pressure apparatus. The sample was subsequently quenched to room temperature, and the pressure was slowly released. A room-temperature synchrotron x-ray powder diffraction (SXRD) pattern was collected using a large Debye−Scherrer camera installed at the BL02B2 beamline of SPring-8, with an x-ray wavelength of 0.7995 Å, 2θ range of 2°–60°, and a step size of 0.006°. Neutron powder diffraction (NPD) patterns were collected with time-of-flight diffractometers performed at the general-purpose powder diffractometer (GPPD) installed at the China Spallation Neutron Source (CSNS) [17]. The Rietveld refinements for the SXRD and NPD data were performed using the GSAS [18] and FULLPROF [19] programs, respectively. During the refinement of the antisite disordered model, specific crystallographic constraints were applied to the site occupation factors to strictly conserve the nominal chemical composition of $CaZnFe_2O_5$. The total amounts of Fe and Zn distributed across the 4*a* and 8*f* Wyckoff sites were constrained to 2.0 and 1.0 per formula unit (f.u.), respectively. Correspondingly, the sum of the fractional occupancies of Fe and Zn at each individual Wyckoff site was fixed to 1.0 for both the 4*a* and 8*f* positions. Furthermore, to maintain a consistent local chemical environment, the atomic displacement parameters (thermal factors) of the co-occupying Zn and Fe atoms at the same Wyckoff site were constrained to be identical. The soft x-ray absorption spectroscopy (XAS) at the Fe-$L_{2,3}$ edge was measured with total electron yield at the BL08B beamline of the National Synchrotron Radiation Research Center (NSRRC) in Taiwan. The spectra were recorded at room temperature with an energy resolution of $\leqslant$0.1 eV using the total electron yield (TEY) mode, obtained by measuring the drain current from the fresh cross-section of a polycrystalline bulk sample. The random crystallite orientation inherently provides a macroscopically isotropic spectrum, free of linear dichroism artifacts. Fe-$L_{2,3}$-edge XAS

spectra were simulated using a configuration-interaction cluster model implemented in the XTLS 9.0 program [20]. The ground state included $3d^5$, $3d^6\underline{L}$, and $3d^7\underline{L}^2$ configurations to fully account for multiplet interactions and Fe-$3d$ to O-$2p$ hybridization. To capture the distinct local environments, the crystal-field and hybridization parameters (V) for the $4a$ and $8f$ sites were individually scaled based on their neutron-refined Fe–O bond lengths d following Harrison's rule $V \sim d^{-3.5}$. The magnetic susceptibility and magnetization were measured with a superconducting quantum interference device (SQUID) magnetometer (Quantum Design, MPMS 3). First-principles calculations were performed within density functional theory using the Perdew–Burke–Ernzerhof form of the generalized gradient approximation (GGA), as implemented in VASP [21,22]. On-site Coulomb interactions were treated using the GGA + U method [23], with $U_{\mathrm{Fe}} = 5$ eV, $U_{\mathrm{Cu}} = 8$ eV, and $J_{\mathrm{H}} = 0.9$ eV, consistent with values used in previous studies [24–26]. A plane-wave cutoff energy of 480 eV and a $5 \times 3 \times 3$ Γ-centered k-point mesh were employed for a $1 \times 2 \times 1$ supercell. The Wigner-Seitz radii for Ca, Cu, Zn, Fe, and O were chosen to be 1.746, 1.164, 1.270, 1.302, and 0.820 Å, respectively. For each compound, the defect-free *Cmcm* structure was compared with a representative antisite configuration generated by exchanging one M ion (M = Zn or Cu) at a $4a$ site with one Fe ion at an $8f$ site. The internal atomic positions were relaxed while the lattice parameters were fixed. The electronic and ionic convergence criteria were 10^{-7} eV and 10^{-3} eV/Å, respectively. The Heisenberg Hamiltonian for magnetic structures without antisite disorder was solved on the mean-field level as previously reported [15]. For the Hamiltonian with antisite disorder, we construct a crystalline supercell with dimensions of $100 \times 1 \times 1$ and calculate the total energy numerically as the sum of all exchange interactions.

III. RESULTS AND DISCUSSION

Figure 1(c) shows the SXRD pattern of $CaZnFe_2O_5$ measured at 300 K. All the diffraction peaks can be well indexed with the orthorhombic space group *Cmcm*, the same one previously reported for $CaFe_3O_5$ [13,16] and $CaCuFe_2O_5$ [15]. The schematic diagram of the crystal structure of the nominal postspinel structure $CaZnFe_2O_5$ is shown in Fig. 1(a). The edge-shared FeO_6 octahedra form one-dimensional Fe_2O_5 zigzag ladders running along the structural a direction [see Fig. 1(b)], which are further connected with each other through corner-shared octahedra with a 133° Fe–O–Fe bond angle along the c axis. Along the b direction, the obtained 2D Fe_2O_5 zigzag ladders are stacked and separated by ZnO_6 chains constituting edge-shared ZnO_6 octahedra with compressed distortion [Figs. 1(a) and 1(b)]. In this case, the magnetism is expected to be 2D, which, however, can be disrupted in the presence of Fe and Zn antisite disorder. To test this possibility, we attempted to refine the SXRD data using a Zn and Fe antisite disordered model. The resulting improvement in the refinement was marginal [see Figs. 1(c) and 1(d)], since the x-ray cross sections for Fe and Zn are quite similar. To further test the presence of antisite disorder, we performed NPD in parallel. Figures 1(e) and 1(f) display the 300 K NPD pattern refined without and with antisite disorder,

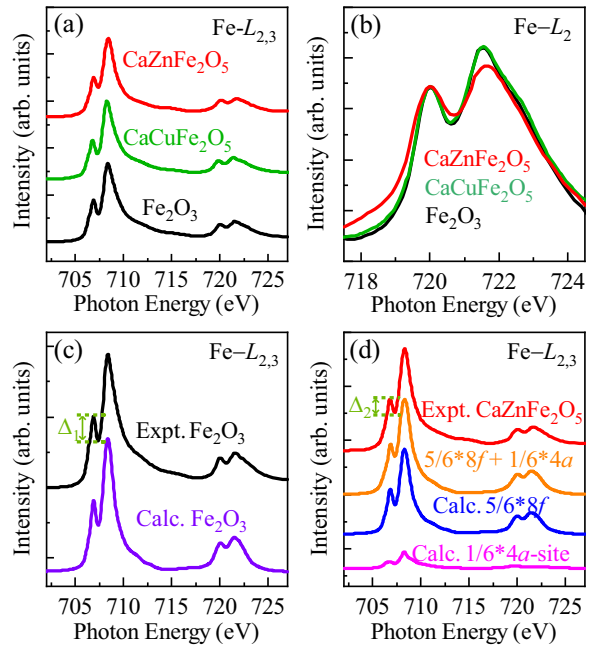

FIG. 2. (a) Fe-L-edge XAS for $CaZnFe_2O_5$ (red) along with $CaCuFe_2O_5$ (green) and Fe_2O_3 (black) as references. (b) Enlarged XAS at the Fe-L_2 edge, with the left peak aligned. Experimental and calculated Fe-$L_{2,3}$-edge XAS spectra. (c) Comparison of the experimental (black) and calculated (purple) Fe-$L_{2,3}$-edge XAS spectra for the single-site reference compound Fe_2O_3, showing sharp multiplet features. (d) Site-dependent spectral simulation for the disordered $CaZnFe_2O_5$. The bottom curves represent the individual calculated spectra for Fe^{3+} residing at the $8f$ site (blue) and the $4a$ site (pink), weighted by their refined site occupancies (5/6 and 1/6, respectively). * in panel (d) denotes multiplication by the corresponding refined site occupancy. Their linear superposition yields the total calculated spectrum (orange line), which well reproduces the experimental data (red line). Δ_1 in panel (c) and Δ_2 in panel (d) represent the spectral valleys at the Fe-L_3 edge of Fe_2O_3 and $CaZnFe_2O_5$, respectively.

respectively. Overall, the NPD data can be well described by the lattice structure determined from the SXRD pattern. However, compared with the refinement performed without antisite disorder ($R_{\mathrm{wp}} = 8.81\%$), the one with Zn and Fe antisite occupations ($R_{\mathrm{wp}} = 3.93\%$) yields a remarkably improved fitting to the nuclear diffraction peaks, particularly for the peaks at $d = 5.0$ and $d = 6.4$ Å [see the fitting in the pink square region in Figs. 1(e) and 1(f)]. Based on the NPD results, a Zn to Fe antisite ratio of 2 : 1 is indicated. In other words, 1/3 of the Zn sites (Wyckoff position $4a$, tetragonally compressed octahedral field) are occupied by Fe, and correspondingly, 1/6 of the Fe sites ($8f$, irregular octahedral field) are occupied by Zn. The refined structure parameters are presented in Table I.

The presence of Zn and Fe antisite disorder can be further inspected by Fe-L-edge XAS, which is highly sensitive to both the valence state and the local crystal field [27–29]. Figure 2(a) displays the Fe-L-edge XAS spectra of $CaZnFe_2O_5$, together with those of Fe_2O_3 and $CaCuFe_2O_5$, which serve as high-spin Fe^{3+} references. The close similarity of the three spectra demonstrates that all Fe atoms in $CaZnFe_2O_5$ adopt a single high-spin Fe^{3+} configuration ($S = 5/2$). A more detailed inspection of the L_2-edge regime, however, reveals

TABLE I. Refined crystal parameters of $CaZnFe_2O_5$ with antisite disorder based on SXRD and NPD diffraction patterns at 300 and 5 K. $(Zn/Fe)_{4a}$ are located at (0, 0, 0) and the x-coordinates of all atoms are fixed at 0 under the symmetry constraint of the *Cmcm* space group. The z coordinates of Ca and O1 atoms are fixed to 0.25. G represents the site occupancy.

Parameter	300 K SXRD	300 K NPD	5 K NPD
a (Å)	3.0186(2)	3.0216(4)	3.0147(2)
b (Å)	10.0305(4)	10.0400(1)	10.0335(7)
c (Å)	12.6689(4)	12.6846(2)	12.6686(3)
Ca_y	0.5208(4)	0.5174(9)	0.5152(3)
$[(Zn/Fe)_{8f}]_y$	0.2688(8)	0.2709(3)	0.2686(9)
$[(Zn/Fe)_{8f}]_z$	0.1099(5)	0.1117(1)	0.1121(6)
$O1_y$	0.1916(4)	0.1931(5)	0.1934(7)
$O2_y$	0.6436(3)	0.6422(8)	0.6429(4)
$O2_z$	0.4497(2)	0.4508(1)	0.4486(3)
$O3_y$	0.8986(3)	0.9092(4)	0.9090(9)
$O3_z$	0.1371(6)	0.1341(9)	0.1346(3)
$G(Zn/Fe)_{4a}$	0.6390(6)/0.3610(6)	0.6583(2)/0.3417(2)	0.6371(5)/0.3629(5)
$G(Zn/Fe)_{8f}$	0.1805(6)/0.8195(6)	0.1709(2)/0.8291(2)	0.1815(5)/0.8185(5)
B_{iso} for Ca (Å^2)	0.586(4)	0.691(9)	0.416(1)
B_{iso} for $(Zn/Fe)_{4a}$ (Å^2)	0.610(1)	0.775(8)	0.604(5)
B_{iso} for $(Zn/Fe)_{8f}$ (Å^2)	0.584(1)	1.089(3)	0.949(7)
B_{iso} for O1 (Å^2)	0.626(9)	0.738(8)	0.210(4)
B_{iso} for O2 (Å^2)	0.767(7)	1.011(5)	0.856(5)
B_{iso} for O3 (Å^2)	0.708(8)	1.082(5)	0.923(9)
$(Zn/Fe)_{8f}$–O1 (×1) (Å)	1.935(1)	1.920(3)	1.902(3)
$(Zn/Fe)_{8f}$–O2 (×2) (Å)	2.104(2)	2.141(2)	2.111(2)
$(Zn/Fe)_{8f}$–O2 (×1) (Å)	2.212(7)	2.219(4)	2.253(4)
$(Zn/Fe)_{8f}$–O3 (×2) (Å)	2.023(2)	2.071(2)	2.082(6)
$(Zn/Fe)_{4a}$–O2 (×2) (Å)	2.014(2)	1.929(3)	1.934(1)
$(Zn/Fe)_{4a}$–O3 (×4) (Å)	2.181(4)	2.170 (3)	2.180(3)
$\angle(Zn/Fe)_{8f}$–O1–$(Fe/Zn)_{8f}$ (deg)	132.86(5)	131.99(1)	133.25(2)
$\angle(Zn/Fe)_{8f}$–O2–$(Fe/Zn)_{4a}$ (deg)	90.16(2)	90.71(6)	90.48(1)
$\angle(Zn/Fe)_{8f}$–O2–$(Fe/Zn)_{4a}$ (deg)	174.46(4)	174.26(7)	174.70(7)
$\angle(Zn/Fe)_{8f}$–O2–$(Fe/Zn)_{4a}$ (deg)	87.57(2)	89.33(4)	87.48(8)

a noticeably broader line shape for $CaZnFe_2O_5$ compared with the reference compounds [see Fig. 2(b)]. This is because, for the disorder-free $CaCuFe_2O_5$, all the Fe^{3+} ions reside at the $8f$ sites, giving rise to narrow and well-defined XAS features [15]. By contrast, in $CaZnFe_2O_5$, the Fe^{3+} ions occupy both the $4a$ and $8f$ sites in distinct crystalline environments, resulting in multiple L_2-edge XAS features. The sum of two sites leads to the poorly resolved XAS spectral profile [30,31]. Similarly, the Fe^{3+} ions at the $4a$ sites contribute extra spectral weight to the L_3-edge XAS, leading to a shallower valley compared with the single-site Fe_2O_3 ($\Delta_2 < \Delta_1$) [see Figs. 2(c) and 2(d)]. Similar disorder-induced reshaping of XAS profiles has also been well-documented in cation-inverted spinels such as $ZnFe_2O_4$ and $MgAl_2O_4$, where the redistribution of cations over inequivalent local environments systematically modifies the spectral features [32,33]. To further verify this, we performed site-dependent charge-transfer multiplet calculations, which indeed demonstrate that with the antisite disorder considered, the spectral valley is effectively reduced [see Figs. 2(c) and 2(d)]. These results further support the pronounced Zn and Fe antisite disorder as revealed by neutron-diffraction refinements.

Now that the Zn and Fe antisite disorder has been well established in $CaZnFe_2O_5$, we examine its impact on the magnetism. Figure 3(a) shows the temperature-dependent magnetic susceptibility of $CaZnFe_2O_5$. Upon cooling, the susceptibility rises significantly, and the zero-field-cooling (ZFC) and field-cooling (FC) modes diverge below $T_N \approx 190$ K [see Fig. 3(a) and the inset]. Consistent with this behavior, the inverse ZFC susceptibility χ^{-1} in Fig. 3(b) exhibits an evident slope change around T_N. Above 220 K, the susceptibility follows the Curie-Weiss (CW) law with a Curie constant $C = 7.85(4)$ (emu K mol^{-1} Oe^{-1}) and an effective moment $\mu_{eff} = 7.92(2)\mu_B$ f.u.$^{-1}$ which is comparable with the spin-only value of 8.37 μ_B/f.u. [see Fig. 3(c)]. Additionally, the fit yields a CW temperature of $\theta_{CW} \approx -316(2)$ K with a frustration factor $f = |\theta_{CW}|/T_N \approx 1.66$. Compared with $CaCuFe_2O_5$ with $f = 12.15$, the markedly reduced frustration factor in the current $CaZnFe_2O_5$ indicates that Zn and Fe antisite disorder releases the magnetic frustration of the Fe_2O_5 zigzag ladders. To determine the nature of the magnetism, we performed isothermal magnetization measurements at various temperatures [see Fig. 3(d)]. Above T_N, the magnetization exhibits linear paramagnetic behaviors, whereas at low temperatures ($<T_N$), small hysteresis without reaching saturation is observed. This behavior indicates a weak ferromagnetic (FM) component accompanying the AFM state.

To elucidate the detailed spin structure, we collected NPD patterns at different temperatures. Although no extra reflections can be observed in the 5 K NPD pattern compared

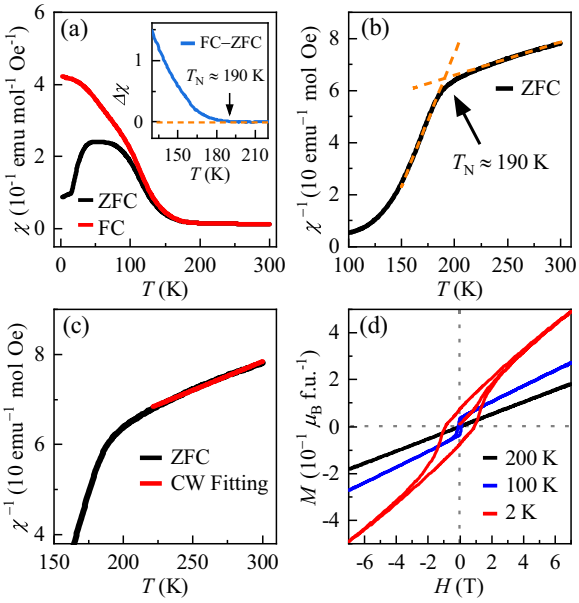

FIG. 3. (a) Temperature-dependent magnetic susceptibility measured at 0.1 T in ZFC and FC modes. The inset shows the difference between the FC and ZFC curves. The dashed line is a guide for the eye. (b) Inverse susceptibility χ^{-1} of the ZFC data, from which T_N is estimated using the tangent construction. (c) Curie–Weiss fitting for the χ^{-1} data between 220 and 300 K using the formula $1/\chi = (T - \theta_{CW})/C$. (d) Field-dependent magnetization measured at various temperatures.

with the 300 K data, several peaks become markedly more intense at 5 K and their intensities decrease monotonically with increasing temperature [see Fig. 4(a)]. This behavior is characteristic of a $\boldsymbol{k} = (0,0,0)$ magnetic structure, for which magnetic Bragg peaks are superimposed on the nuclear ones. Figure 4(b) displays the Rietveld refinement of the 5 K NPD pattern (the refined structural parameters are presented in Table I), and the resulting magnetic structure is illustrated in Fig. 4(d). During the refinement of 5 K NPD data, a uniform b axis FM component of $M_b \approx 0.10\mu_B$ per Fe^{3+} was imposed, which was estimated from the 2 K magnetization curve. This constraint is necessary considering that the FM component is very small and contributes only marginally to the powder-averaged diffraction intensity, making it unreliable to determine from the NPD data independently. The final refinement model exhibits a canted A-type AFM arrangement. The AFM component, which dominates the magnetic order, features Fe^{3+} moments running along the c axis, constituting FM $8f$-site zigzag ladders and $4a$-site chains coupled antiferromagnetically to each other. The refined principal c axis component is $M_c = 2.178(9)\mu_B$ per Fe^{3+}, which is smaller than the spin-only value expected for high-spin Fe^{3+}. This reduction may be associated with the Zn and Fe antisite disorder, which leads to statistical averaging of the macroscopic magnetization contributed by Fe^{3+}. Combining the principal c axis component with the b axis FM component yields an approximate canting angle of 2.6°, which is fixed during the refinement of NPD patterns of other temperatures.

Within this canting picture, the weak FM component may be rationalized by Dzyaloshinskii–Moriya (DM) interactions [34–36], which arise from the broken spatial inversion symmetry between neighboring $8f$-site zigzag ladders [see Fig. 4(d)]. According to the DM Hamiltonian $H_{DM} = \boldsymbol{D} \cdot (S_1 \times S_2)$ and symmetry rule, the allowed $\boldsymbol{D}$ vector is along the a axis, which would favor a canting component along the b axis [37,38].

As the temperature is raised, the static ordered moment diminishes continuously and vanishes near T_N [Fig. 4(c)]. Note that the refined nuclear structural parameters at 5 K, including the Zn and Fe antisite occupancy, are similar to those obtained at 300 K (see Table I). The refined M_c values of Fe^{3+} and the corresponding M_b components calculated using the fixed canting angle at different temperatures are shown in Table II.

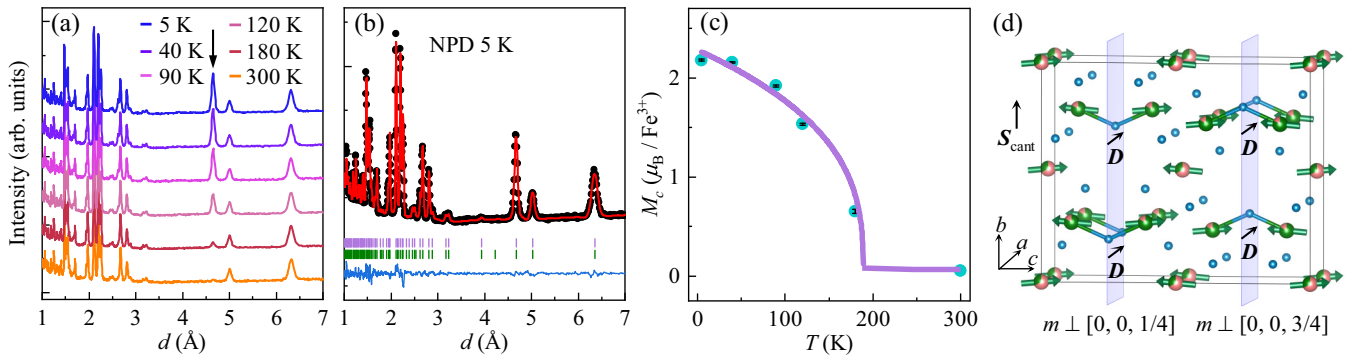

FIG. 4. (a) NPD patterns of $CaZnFe_2O_5$ collected at different temperatures. The black arrow highlights the strongest magnetic Bragg peak $Q = (0,2,1)$ that overlaps with a weak nuclear peak. (b) NPD refinement results obtained at 5 K with antisite disorder considered. The observed (black dot), calculated (red line), and difference (blue line) profiles are shown. The purple and green ticks indicate the allowed nuclear and magnetic reflections, respectively. (c) Temperature dependence of the NPD refined principal c axis ordered moment M_c of Fe^{3+}. Note that the error bars are smaller than the data points. The solid line represents the fitting result of the power-law critical behavior using the formula $M = M_0(1-T/T_N)^{\beta}$, which gives zero-temperature ordered moment $M_0 = 2.28(9)\mu_B$ per Fe^{3+}, Néel temperature $T_N = 189(9)$ K, and order-parameter exponent $\beta = 0.32(7)$. (d) Schematic of the A-type magnetic structure obtained from the NPD refinement for $CaZnFe_2O_5$ with antisite disorder, in which the $\boldsymbol{D}$ vector corresponding to the 133° Fe–O–Fe angle is also shown. The Zn, Fe, and O atoms are represented by pink, green, and blue colors, respectively. The bridging oxygen atoms break spatial inversion symmetry and lie on the mirror plane [0,0,1/4] and [0,0,3/4].

TABLE II. Temperature dependence of the Fe^{3+} ordered moment in $CaZnFe_2O_5$. M_c is the principal c axis component obtained from the NPD refinement independently. The b axis component M_b at 5 K is estimated from the magnetization data, and the values for other temperatures are obtained by assuming the same canting angle as that at 5 K.

Parameter	300 K	180 K	120 K	90 K	40 K	5 K
$M_b(\mu_B$ /$Fe^{3+})$	0	0.030	0.070	0.088	0.099	0.100
$M_c(\mu_B/Fe^{3+})$	0	0.651(19)	1.533(11)	1.919(10)	2.155(9)	2.178(9)

Our NPD refinement shows that the $8f$-site zigzag ladders in $CaZnFe_2O_5$ are ferromagnetically ordered. This differs from the AFM ladders reported for $CaCuFe_2O_5$ [15] and for stoichiometric site-ordered $CaFe_3O_5$ [13,16], but is similar to the $\boldsymbol{k} = (0, 0, 0)$ charge-averaged phase reported in nominal $CaFe_3O_5$. The G-type magnetic structure in stoichiometric $CaFe_3O_5$ is tied to Fe^{2+}, Fe^{3+} charge ordering and the accompanying structural distortion. Such a charge-ordered state is not expected in $CaZnFe_2O_5$, since the Fe-L-edge XAS results show that the Fe ions are all high-spin Fe^{3+}, and NPD refinement indicates that Fe^{3+} ions occupy both the $8f$ and the $4a$ sublattices. Therefore, $CaZnFe_2O_5$ is more closely related to the charge-averaged phase of $CaFe_3O_5$ than to the stoichiometric charge-ordered phase. To further understand the microscopic origin of this A-type order, we now consider how Zn and Fe antisite disorder modifies the magnetic exchange network. In the nominal postspinel structure without antisite disorder [see Fig. 1(a)], the FeO_6 zigzag spin ladders are separated by nonmagnetic ZnO_6 blocks, producing a quasi-2D magnetic network. Considering the isotropic intraleg (J_1) and interleg (J_2) exchange interactions within the ladders, our mean-field calculations predict an IC magnetic structure with a propagation vector of $\boldsymbol{k} = (k_a, 0, 0)$, in which k_a depends on the ratio J_1/J_2 [see Figs. 5(b) and 5(d)]. Note that the interladder exchange interaction J_{133° is predominantly AFM and unfrustrated [39], and DM interactions are not considered in this model for simplicity. In the real material, antisite disorder places magnetic Fe^{3+} ions on a fraction of the $4a$ sites. These Fe^{3+} ions bridge the otherwise isolated 2D sheets, turning the magnetic lattice into a 3D network. Geometric frustration arises from the competition among intraladder and interchain-ladder exchange interactions, leading to two competing magnetic configurations: A-type order with FM ladders [see Fig. 5(a)] and G-type order with AFM ladders proposed for site-ordered $CaFe_3O_5$ [see Fig. 5(c)] [13]. To elucidate such competition, we calculated the total energy of these two configurations as a function of the ratio of in-plane (J_{in}) and out-of-plane (J_{out}) exchange interactions. Here, both J_{in} and J_{out} are AFM. The calculations reveal that when $J_{\text{in}}/J_{\text{out}} > 0.5$, the G-type configuration has the lower total energy [see Fig. 5(e)]. However, when $J_{\text{in}} / J_{\text{out}} < 0.5$, the stronger J_{out} overwhelms J_{in}, forcing the spins to be aligned parallel to each other within the ladders and stabilizing the A-type structure. This observation proves that FM spin ladders can be realized despite the AFM exchange interactions. Our calculations also indicate that the presence of antisite disorder is essential for achieving the A-type magnetic structure observed for $CaZnFe_2O_5$. This illustrates how antisite disorder can reshape the magnetic ground state of postspinel oxides. Given the pronounced Zn and Fe antisite disorder, a fully quantitative microscopic treatment would require explicit configurational sampling of disordered supercells. Different local antisite arrangements can produce markedly different exchange pathways and magnetic energies, making it difficult for calculations based on a limited set of supercell models to yield unique and quantitatively robust exchange parameters. Such calculations are beyond the scope of current work, and our approach offers a qualitative framework for rationalizing the observed A-type magnetic ground state.

Now we discuss the microscopic thermodynamic origin of the pronounced Zn and Fe antisite disorder in $CaZnFe_2O_5$ versus its absence in $CaCuFe_2O_5$. The site preference of transition-metal cations in such mixed-site systems is governed by the total Gibbs free energy ($\Delta G = \Delta H_{\text{size}} + \Delta H_{\text{JT}} - T\Delta S$). Here, ΔH_{size} accounts for the ionic size mismatch effects, meaning that site mixing is favored if two constituent ions have similar radii. In the title compound, the mismatch between Zn^{2+} (0.74 Å) and high-spin Fe^{3+} (0.645 Å) is comparable to that between Cu^{2+} (0.73 Å) and Fe^{3+}. However, no site-mixing is present in $CaCuFe_2O_5$, excluding ionic size mismatch as the primary origin of site mixing observed here. Other factors, such as covalency, could play a role, although their impact is expected to be minimal. Additionally, as mentioned above, the crystal structure of $CaZnFe_2O_5$ contains two crystallographically distinct octahedral sites: the $4a$ sites that are strongly compressed, and the $8f$ sites experiencing only modest distortion. For $CaZnFe_2O_5$, Zn^{2+} ($t_{2g}^6 e_g^4$) and high-spin Fe^{3+} ($t_{2g}^3 e_g^2$) possess fully filled and half-filled $3d$ shells, respectively. Consequently, both ions adopt a spherically symmetric electron configuration, yielding a crystal-field stabilization energy (CFSE) of exactly zero in any octahedral environment, regardless of the local structural distortion, and therefore neither ion is JT active. Thus, there is no electronic driving force (ΔH_{JT}) that preferentially stabilizes one site over the other for either ion, making the Zn and Fe antisite disorder possible, governed by configurational entropy and potentially thermodynamic free-energy ($-T\Delta S$) gain at high temperatures [40,41].

In contrast, the Cu^{2+} ($t_{2g}^6 e_g^3$) ion in $CaCuFe_2O_5$ is strongly JT-active, which gains a massive CFSE and lowers the energy of Cu^{2+} when it resides in the highly compressed $4a$-site octahedra. This provides a substantial electronic stabilization that outweighs the entropic gain from disorder [42,43]. As a result, Cu^{2+} almost exclusively occupies the $4a$ sites, suppressing any type of antisite disorder. An intermediate scenario applies to $CaFe_3O_5$, for which the high-spin Fe^{2+} ($t_{2g}^4 e_g^2$) ion is weakly JT active. The modest energy advantage of placing Fe^{2+} at the $4a$ sites competes with the entropy-driven tendency toward antisite disorder, giving rise to a mixed behavior: both a site-ordered phase and a disordered phase with partial

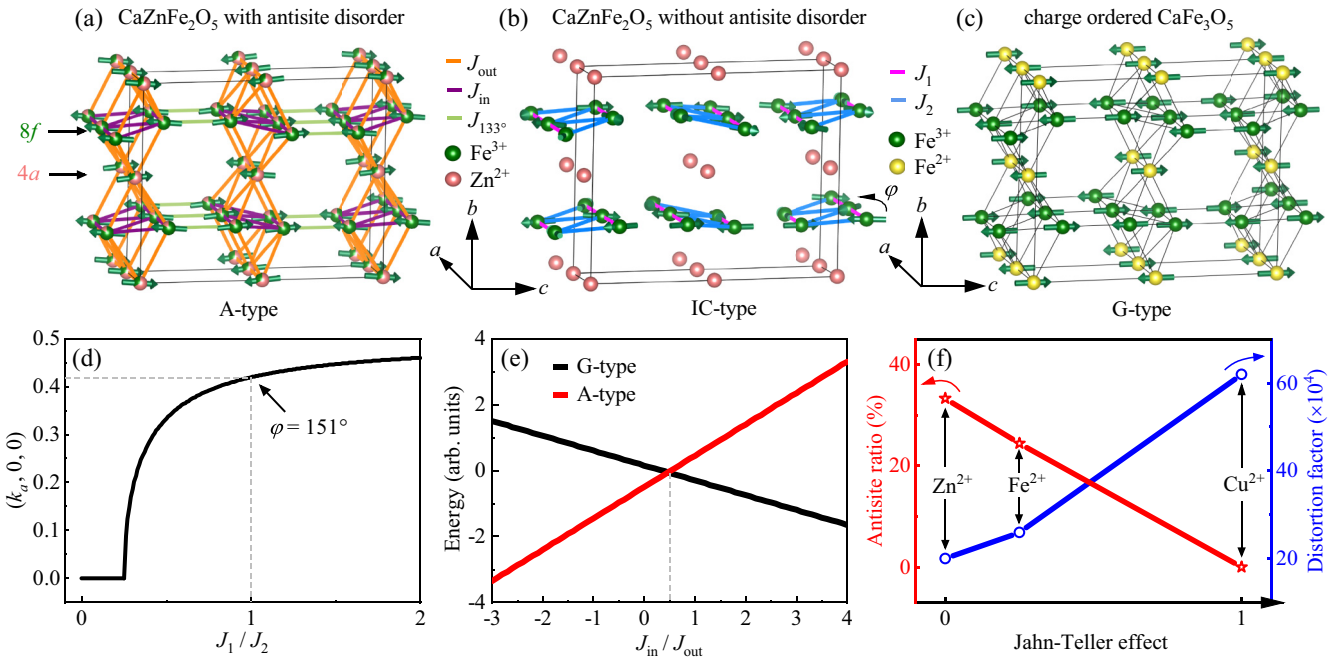

FIG. 5. (a) Schematic of the three main exchange interactions within the A-type magnetic structure for $CaZnFe_2O_5$ with antisite disorder. (b) Incommensurate (IC) magnetic structure expected for $CaZnFe_2O_5$ in the absence of antisite disorder. Note that φ is the angle between adjacent moments within the zigzag spin ladder. Note that we fix $J_1 = J_2 = J_{in}$ when modeling the A-type spin structure. (c) G-type magnetic structure of stoichiometric charge-ordered $CaFe_3O_5$ ($CaFe^{2+}Fe^{3+}_2O_5$). (d) Calculated propagation vector against the exchange interaction ratio J_1/J_2 for the IC-type magnetic structure. The dashed lines indicate the scenario when $J_1/J_2 = 1$. (e) Calculated total energies of A-type and G-type spin structures as a function of J_{in}/J_{out} for $CaZnFe_2O_5$ with antisite disorder. These two structures become degenerate for $J_{in}/J_{out} = 0.5$, highlighted by the dashed line. (f) Jahn-Teller effect dependent antisite ratio (red line) and distortion factor (blue line) of $CaMFe_2O_5$ ($M = Zn^{2+}$, Fe^{2+}, or Cu^{2+}). The distortion factor is defined as $\Delta = \sum[(d_i - d_0)/d_0]^2/6$, where d_i is the metal-ligand distance and d_0 is the average distance.

antisite occupations have been reported for $CaFe_3O_5$. Figure 5(f) summarizes the correlation among the JT effect, antisite ratio, and distortion factors of the MO_6 octahedra of $CaMFe_2O_5$ ($M = Zn^{2+}$, Fe^{2+}, or Cu^{2+}). The absence of JT effect for Zn^{2+} removes any energetic penalty for occupying the more distorted 4*a* sites, leading to the highest antisite fraction, whereas strong JT activity for Cu^{2+} enforces site selectivity and eliminates disorder [44,45].

To provide a quantitative energetic test of this interpretation, we performed GGA + *U* supercell calculations for $CaZnFe_2O_5$ and $CaCuFe_2O_5$ (see Fig. 6). The calculated total energy increase upon antisite defect is 89 meV/f.u. for $CaZnFe_2O_5$, whereas it is 340 meV/f.u. for $CaCuFe_2O_5$. Given the high-pressure and high-temperature synthesis conditions, one may estimate the amount of antisite defects as $\exp(-\Delta E/k_BT)$, which yields approximately 40% antisite defects in $CaZnFe_2O_5$ and approximately 3% in $CaCuFe_2O_5$. This pronounced contrast quantitatively supports the stronger site preference of JT active Cu^{2+} and the substantially lower energetic penalty for Zn and Fe antisite disorder in $CaZnFe_2O_5$.

IV. CONCLUSIONS

In summary, we have successfully synthesized the post-spinel oxide $CaZnFe_2O_5$ and systematically explored the intimate relationship between lattice disorder and magnetism. Detailed structural analysis reveals pronounced Zn^{2+} and Fe^{3+} antisite disorder, in sharp contrast with the ordered Cu^{2+} and Fe^{3+} arrangement observed in the analogous $CaCuFe_2O_5$. We attribute this difference to the distinct JT inactivity of the constituent ions. Despite the disorder, $CaZnFe_2O_5$ exhibits long-range AFM order. Heisenberg model simulations show

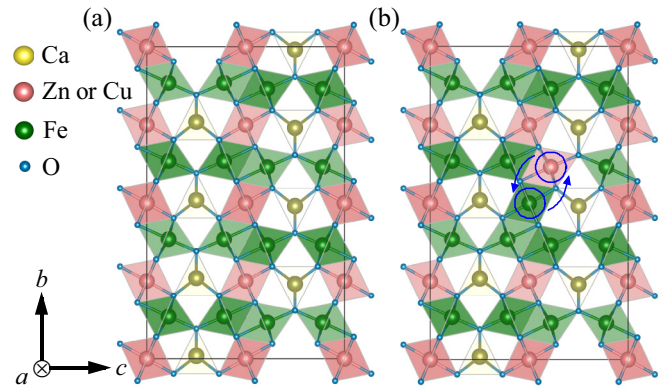

FIG. 6. Crystal structure models used for the first-principles calculations. (a) Defect-free ordered structure of the *Cmcm* phase for $CaMFe_2O_5$ (M = Zn or Cu). (b) Representative antisite defect structure containing a single *M*-Fe antisite exchange pair, where one *M* ion on the 4*a* site and one Fe ion on the 8*f* site are exchanged. The blue circles and arrows mark the exchanged ions and illustrate the antisite exchange process. The calculated energy increases upon antisite defect are 89 meV/f.u. for $CaZnFe_2O_5$ and 340 meV/f.u. for $CaCuFe_2O_5$.

that competing exchange interactions enforce an FM zigzag ladder, even though the intraladder couplings are AFM. Such a magnetic configuration is stabilized by antisite disorder, which disrupts the otherwise incommensurate spin structure, and a net FM moment emerges from DM interactions. Our findings demonstrate how JT inactivity promotes antisite disorder, which, instead of diluting magnetism and suppressing long-range order, reconfigures the spin network by introducing additional exchange competition. Consequently, we establish antisite disorder as a crucial structural parameter that must be considered when analyzing the magnetic properties of materials with a dense structure like postspinel oxides. The correlation between JT inactivity and disorder-induced magnetism further provides a valuable perspective for understanding and designing complex magnetic materials.

ACKNOWLEDGMENTS

The authors thank X. Wang and A. Tanaka for their assistance with the configuration-interaction calculations of the XAS spectra. This work was supported by the National Natural Science Foundation of China (Grants No. 12425403, No. 12574139, No. 12304268, and No. 12304159) and the National Key R&D Program of China (Grant No. 2021YFA1400300), as well as by the China Postdoctoral Science Foundation (Grant No. 2023M743741). The neutron diffraction experiments were supported by the Open Fund of the China Spallation Neutron Source Songshan Lake Science City (Grant No. KFKT2023A08). The synchrotron x-ray powder diffraction experiments were performed at SPring-8 with the approval of the Japan Synchrotron Radiation Research Institute (Grants No. 2024A1506, No. 2024A1695, and No. 2025A1495). We acknowledge support from the Max Planck-POSTECH-Hsinchu Center for Complex Phase Materials. S.V.S. and A.E.L. thank the Ministry of Science and Higher Education of the Russian Federation for support through funding the Institute of Metal Physics.

DATA AVAILABILITY

The data that support the findings of this article are not publicly available because they contain commercially sensitive information. The data are available from the authors upon reasonable request.

[1] H. L. Tuller and S. R. Bishop, Point defects in oxides: Tailoring materials through defect engineering, Annu. Rev. Mater. Res. **41**, 369 (2011).

[2] Y. Zheng, T. J. Slade, L. Hu, X. Y. Tan, Y. Luo, Z.-Z. Luo, J. Xu, Q. Yan, and M. G. Kanatzidis, Defect engineering in thermoelectric materials: What have we learned? Chem. Soc. Rev. **50**, 9022 (2021).

[3] F. A. Kroger, Defect chemistry in crystalline solids, Annu. Rev. Mater. Res. **7**, 449 (1977).

[4] C. Freysoldt, B. Grabowski, T. Hickel, J. Neugebauer, G. Kresse, A. Janotti, and C. G. Van de Walle, First-principles calculations for point defects in solids, Rev. Mod. Phys. **86**, 253 (2014).

[5] M. U. Muzaffar, S. Zhang, P. Cui, J. He, and Z. Zhang, Antisite defect-enhanced thermoelectric performance of topological crystalline insulators, Adv. Funct. Mater. **30**, 2003162 (2020).

[6] R. C. Sahoo, Y. Takeuchi, A. Ohtomo, and Z. Hossain, Exchange bias and spin glass states driven by antisite disorder in the double perovskite compound $LaSrCoFeO_6$, Phys. Rev. B **100**, 214436 (2019).

[7] S. X. M. Riberolles, Q. Zhang, E. Gordon, N. P. Butch, L. Ke, J. Q. Yan, and R. J. McQueeney, Evolution of magnetic interactions in Sb-substituted $MnBi_2Te_4$, Phys. Rev. B **104**, 064401 (2021).

[8] Q. Chen, C. Svoboda, Q. Zheng, B. C. Sales, D. G. Mandrus, H. D. Zhou, J. S. Zhou, D. McComb, M. Randeria, N. Trivedi, *et al.*, Magnetism out of antisite disorder in the $J = 0$ compound Ba_2YIrO_6, Phys. Rev. B **96**, 144423 (2017).

[9] M. E. Zhitomirsky, V. B. Shenoy, and R. Moessner, Defect-induced spin textures in magnetic solids, Phys. Rev. B **111**, 184414 (2025).

[10] A. Kumar, B. Schwarz, and R. S. Dhaka, Correlation between the exchange bias effect and antisite disorder in $Sr_{2-x}La_xCoNbO_6$ ($x = 0,\ 0.2$), Phys. Rev. B **109**, 104434 (2024).

[11] S. Ning, A. Kumar, K. Klyukin, E. Cho, J. H. Kim, T. Su, H.-S. Kim, J. M. LeBeau, B. Yildiz, and C. A. Ross, An antisite defect mechanism for room temperature ferroelectricity in orthoferrites, Nat. Commun. **12**, 4298 (2021).

[12] X. Hu, X. He, Z. Guo, T. Kamiya, and J. Wu, Antisite-defects control of magnetic properties in $MnSb_2Te_4$, ACS Nano **18**, 738 (2024).

[13] S. J. Cassidy, F. Orlandi, P. Manuel, and S. J. Clarke, Single phase charge ordered stoichiometric $CaFe_3O_5$ with commensurate and incommensurate trimeron ordering, Nat. Commun. **10**, 5475 (2019).

[14] S. V. Ovsyannikov, M. Bykov, E. Bykova, D. P. Kozlenko, A. A. Tsirlin, A. E. Karkin, V. V. Shchennikov, S. E. Kichanov, H. Gou, and A. M. Abakumov, Charge-ordering transition in iron oxide Fe_4O_5 involving competing dimer and trimer formation, Nat. Chem. **8**, 501 (2016).

[15] M. Pi, J. Yang, J. Zhang, X. Ye, X. Wang, L. He, Z. Hu, C.-T. Chen, C. Kuo, Z. Pan, *et al.*, Observation of robust compressed CuO_6 octahedra and exotic spin structure in $CaCuFe_2O_5$, J. Am. Chem. Soc. **147**, 4403 (2025).

[16] K. H. Hong, A. M. Arevalo-Lopez, J. Cumby, C. Ritter, and J. P. Attfield, Long range electronic phase separation in $CaFe_3O_5$, Nat. Commun. **9**, 2975 (2018).

[17] L. He, S. Deng, F. Shen, J. Chen, H. Lu, Z. Tan, H. Zheng, J. Hao, D. Zhao, and Q. Ma, The performance of general purpose powder diffractometer at CSNS, Nucl. Instrum. Methods. Phys. Res. A **1054**, 168414 (2023).

[18] B. H. Toby, *EXPGUI*, a graphical user interface for *GSAS*, J. Appl. Crystallogr. **34**, 210 (2001).

[19] J. Rodríguez-Carvajal, Recent advances in magnetic structure determination by neutron powder diffraction, Physica B **192**, 55 (1993).

[20] A. Tanaka and T. Jo, Resonant 3*d*, 3*p* and 3*s* photoemission in transition metal oxides predicted at 2*p* threshold, J. Phys. Soc. Jpn. **63**, 2788 (1994).

[21] G. Kresse and D. Joubert, From ultrasoft pseudopotentials to the projector augmented-wave method, Phys. Rev. B **59**, 1758 (1999).

[22] J. P. Perdew, K. Burke, and M. Ernzerhof, Generalized gradient approximation made simple, Phys. Rev. Lett. **77**, 3865 (1996).

[23] A. Liechtenstein, V. I. Anisimov, and J. Zaanen, Density-functional theory and strong interactions: Orbital ordering in Mott-Hubbard insulators, Phys. Rev. B **52**, R5467 (1995).

[24] I. S. Zhidkov, A. A. Belik, A. I. Kukharenko, S. O. Cholakh, L. S. Taran, A. Fujimori, S. V. Streltsov, and E. Kurmaev, Cu-site disorder in $CuAl_2O_4$ as studied by XPS spectroscopy, JETP Lett. **114**, 556 (2021).

[25] A. Shorikov, M. Korotin, S. Streltsov, S. Skornyakov, D. M. Korotin, and V. Anisimov, Coulomb correlation effects in LaFeAsO: An LDA+ DMFT (QMC) study, J. Exp. Theor. Phys. **108**, 121 (2009).

[26] Z. Pchelkina and S. Streltsov, *Ab initio* investigation of the exchange interactions in $Bi_2Fe_4O_9$: The Cairo pentagonal lattice compound, Phys. Rev. B **88**, 054424 (2013).

[27] N. Hollmann, M. Valldor, H. Wu, Z. Hu, N. Qureshi, T. Willers, Y.-Y. Chin, J. Cezar, A. Tanaka, and N. Brookes, Orbital occupation and magnetism of tetrahedrally coordinated iron in $CaBaFe_4O_7$, Phys. Rev. B **83**, 180405 (2011).

[28] H. Deng, M. Liu, J. Dai, Z. Hu, C. Kuo, Y. Yin, J. Yang, X. Wang, Q. Zhao, and Y. Xu, Strong enhancement of spin ordering by A-site magnetic ions in the ferrimagnet $CaCu_3Fe_2Os_2O_{12}$, Phys. Rev. B **94**, 024414 (2016).

[29] T. Burnus, Z. Hu, H. Wu, J. Cezar, S. Niitaka, H. Takagi, C. F. Chang, N. B. Brookes, H.-J. Lin, and L. Jang, X-ray absorption and x-ray magnetic dichroism study on Ca_3CoRhO_6 and Ca_3FeRhO_6, Phys. Rev. B **77**, 205111 (2008).

[30] B. A. Rosales, L. Men, S. D. Cady, M. P. Hanrahan, A. J. Rossini, and J. Vela, Persistent dopants and phase segregation in organolead mixed-halide perovskites, Chem. Mater. **28**, 6848 (2016).

[31] F. Farges, Coordination of Ti^{4+} in silicate glasses: A high-resolution XANES spectroscopy study at the Ti K edge, Am. Mineral. **82**, 36 (1997).

[32] S. Yoshioka, K. Tsuruta, T. Yamamoto, K. Yasuda, S. Matsumura, N. Ishikawa, and E. Kobayashi, X-ray absorption near edge structure and first-principles spectral investigations of cationic disorder in $MgAl_2O_4$ induced by swift heavy ions, Phys. Chem. Chem. Phys. **20**, 4962 (2018).

[33] S. J. Stewart, S. J. A. Figueroa, J. M. Ramallo López, S. G. Marchetti, J. F. Bengoa, R. J. Prado, and F. G. Requejo, Cationic exchange in nanosized $ZnFe_2O_4$ spinel revealed by experimental and simulated near-edge absorption structure, Phys. Rev. B **75**, 073408 (2007).

[34] C. Ederer and N. A. Spaldin, Weak ferromagnetism and magnetoelectric coupling in bismuth ferrite, Phys. Rev. B **71**, 060401 (2005).

[35] V. Mazurenko and V. Anisimov, Weak ferromagnetism in antiferromagnets: *A*-Fe_2O_3 and La_2CuO_4, Phys. Rev. B **71**, 184434 (2005).

[36] V. Skumryev, F. Ott, J. M. D. Coey, A. Anane, J.-P. Renard, L. Pinsard-Gaudart, and A. Revcolevschi, Weak ferromagnetism in $LaMnO_3$, Eur. Phys. J. B **11**, 401 (1999).

[37] I. Dzyaloshinsky, A thermodynamic theory of "weak" ferromagnetism of antiferromagnetics, J. Phys. Chem. Solids **4**, 241 (1958).

[38] T. Moriya, Anisotropic superexchange interaction and weak ferromagnetism, Phys. Rev. **120**, 91 (1960).

[39] J. Goodenough, *Magnetism and the Chemical Bond* (Interscience Publishers, New York, 1963).

[40] A. Šutka, R. Pärna, M. Zamovskis, V. Kisand, G. Mezinskis, J. Kleperis, M. Maiorov, and D. Jakovlev, Effect of antisite defects on the magnetic properties of $ZnFe_2O_4$, Phys. Status Solidi (a) **210**, 1892 (2013).

[41] S. V. Ushakov, S. Hayun, W. Gong, and A. Navrotsky, Thermal analysis of high entropy rare earth oxides, Materials **13**, 3141 (2020).

[42] A. Kyono, S. A. Gramsch, Y. Nakamoto, M. Sakata, M. Kato, T. Tamura, and T. Yamanaka, High-pressure behavior of cuprospinel $CuFe_2O_4$: Influence of the Jahn-Teller effect on the spinel structure, Am. Mineral. **100**, 1752 (2015).

[43] L. Shi, K. Chen, T. Huang, Y. Zhang, Z. Wang, and Q. Zhang, Unraveling the role of Cu^{2+} induced Jahn-Teller distortion and electron occupation alternation in modulating electronic and optical properties of $Cu_xFe_{1-x}Fe_2O_4$, Ceram. Int. **50**, 23937 (2024).

[44] S. Dong, S. Dai, X. Yao, K. Wang, C. Zhu, and J.-M. Liu, Jahn-Teller distortion induced charge ordering in the CE phase of manganites, Phys. Rev. B **73**, 104404 (2006).

[45] R. J. Green, M. W. Haverkort, and G. A. Sawatzky, Bond disproportionation and dynamical charge fluctuations in the perovskite rare-earth nickelates, Phys. Rev. B **94**, 195127 (2016).